

Corrosion of 316L & 316H stainless steel in molten LiF-NaF-KF (FLiNaK)

William Doniger^{a,*}, Cody Falconer^a, Adrien Couet^b, Kumar Sridharan^{a,b}



^a Department of Materials Science and Engineering, University of Wisconsin-Madison, United States

^b Department of Engineering Physics, University of Wisconsin-Madison, United States

ARTICLE INFO

Article history:

Received 30 November 2022

Revised 7 March 2023

Accepted 8 March 2023

Available online 12 March 2023

Keywords:

Molten salt corrosion

FLiNaK

Stainless steel

Sensitization

ABSTRACT

The corrosion behavior of 316L and 316H stainless steels (low and high carbon, respectively) in molten LiF-NaF-KF (FLiNaK) salt at 700 °C for 500 h has been investigated. Tests were performed in 316L stainless steel, pyrolytic boron nitride, and glassy carbon capsule materials. The capsule material had a notable effect on the corrosion behavior of the two stainless steels. The modes of corrosion for the two types of stainless steel in various capsule materials were classified into three categories, namely, uniform surface recession, selective grain boundary Cr dissolution, and the dissolution of Cr in the bulk grains. By most metrics, the 316H stainless steel exhibited slightly superior corrosion resistance, while by others the two stainless steels were comparable. These differences in corrosion behavior are attributed to the differences in grain size and the degree of sensitization.

© 2023 Elsevier B.V. All rights reserved.

1. Introduction

The Molten Salt Reactor (MSR) is being actively pursued as a next-generation nuclear reactor concept because it provides higher passive safety and efficiency, high operation temperature (~700°C), and yields lower fuel waste [1]. The construction of MSRs requires salt-facing structural materials with a combination of high-temperature creep properties, corrosion resistance, and radiation damage tolerance. Type 316 stainless steel, with the nominal composition 16–18 Cr, 10–14 Ni, 2–3 Mo, and 2 Mn (wt. %), is a lead candidate for this application due to its relatively well understood mechanical properties and ready availability. The high carbon variant of this stainless steel, 316H (0.04–0.10 wt. %) is one of the few ASME Boiler and Pressure Vessel Code Section III Division 5 qualified alloys for construction of reactors exceeding in operating temperature of 425 °C [2]. In comparison to other alloys developed for MSRs, however, 316 stainless steel has a relatively high concentration of Cr which, in principle, makes it more prone to corrosion in molten fluoride salts [3]. The ASME code requirements have put new emphasis on investigation of 316 stainless steel for salt facing applications, which historically has not received the same attention as the Ni-based alloys. Consequently, important questions remain regarding the corrosion mechanisms relevant to 316 stainless steels, and the role of minor differences in carbon content, microstructure, and phase stability at high temperatures.

In molten fluorides salts, it is commonly accepted that corrosion occurs by conversion of alloying elements into corresponding dissolved soluble fluorides. In the inevitable presence of trace impurities in the salt, the passivating oxide layer that is usually relied upon for corrosion resistance in other environments is rendered unstable leaving the material exposed to corrosion attack by the molten salt [3]. The propensity of an alloying element to corrosion is governed by its Gibbs free energy of fluoride formation and the redox condition of the molten salt mixture [4]. Chromium, which is required for air side oxidation resistance in most high-temperature structural alloys, readily forms a fluoride compared to most other alloying elements [5]. Consequently, the most commonly observed mode of corrosion attack is selective dealloying of chromium in the near surface region of the alloy [6].

Assessment of the available corrosion data reveals inconsistencies in the possible modes of corrosion attack occurring in 316 stainless steels in molten fluoride salts. It is commonly reported [7–11] that the dominant mode of corrosion is selective dissolution of chromium along grain boundaries. Several studies [12–15] have also reported transport of both Cr and Fe from iron-based alloys via the molten fluoride salt onto the surfaces of nickel, nickel-based alloys, or graphite in static isothermal experiments. Raiman et al. [16] showed the transport of Cr and Fe from hot to cold sections in a thermal flow loop constructed of 316 stainless steel. While the exact mechanisms governing these behaviors is still in question, a common feature of these experiments are dissimilar materials or temperature gradients that may perturb the system, establishing corrosive salt redox conditions. Thus far, degradation by surface recession has not been a focus of most corrosion studies. It is hypothesized that corrosion of Fe from the matrix grains

* Corresponding author.

E-mail address: wdoniger@anl.gov (W. Doniger).

may lead to a mode of corrosion attack more akin to uniform surface recession rather than selective dissolution. Previous electrochemical investigation of the corrosion behavior of metals and alloys by the authors revealed that corrosion of the bulk material was possible under a variety of conditions and that Fe-based alloys were more susceptible to corrosion than Ni-based alloys [17]. Therefore, overlooking uniform surface recession could lead to inaccurate assessments of corrosion rate in molten salts.

An important distinction among commercially available 316 stainless steels that could be relevant to corrosion in MSRs is the carbon concentration. 316H stainless steel (316H) has a slightly higher carbon concentration (0.04–0.10 wt.% C), compared to the more common 316L stainless steel (316L) (<0.03 wt.% C). While the increased carbon is beneficial for mechanical properties at higher temperatures, different corrosion behavior may arise due to the affinity of the carbon for the chromium in solid solution. In a certain high temperature range, sensitization can occur in stainless steels where the carbon reacts with Cr to form a chromium carbide phase at the grain boundaries, leaving behind a Cr denuded zone in the vicinity of the grain boundaries [18]. This microstructural and chemical change at and near the grain boundaries can potentially influence the corrosion behavior in molten fluoride salts.

In this research, the mode of corrosion attack affecting 316L and 316H stainless steel specimens in molten FLiNaK salt at 700 °C was measured in terms of key metrics: weight change, the depth of selective dissolution of an alloying element, and surface recession. With these metrics, distinctions were made between the corrosion occurring in different capsule materials, including 316 stainless steel, pyrolytic boron nitride (PBN), and glassy carbon. SEM and EDS analyses were used to quantify changes in near-surface elemental composition and determine the extent of dissolution of certain alloying elements in the bulk grains and the grain boundaries, while the bulk recession was measured by profilometry of semi-submerged specimens.

2. Experimental

2.1. Materials

Two variants of type 316 stainless steel with low (316L) and high (316H) carbon contents were tested in static corrosion tests in molten salt. A 14-gauge (1.9 mm) 316L sheet was procured from a commercial source. A 12.7 mm-thick plate of 316H was purchased from Sandmeyer Steel. The composition of the two stainless steels were measured by Anderson Laboratory, Inc. to confirm that they were consistent with the specifications. Carbon content of the stainless steels was measured with a Leco CS844, while Leco O/N 736 was used to measure nitrogen concentration. The concentrations of the remaining elements were analyzed using an ARL-Spark OES Metals Analyzer. As shown in Table 1, the 316L and 316H have compositions consistent with the specification of their grade, with the carbon content being slightly higher for 316H. Specimen were cut using wire electrical discharge machining (EDM) to dimensions of approximately 14 mm × 11 mm × 1.5 mm. Two 1.58 mm diameter holes were drilled in each end of the specimen to facilitate

Table 1
316L and 316H stainless steels specifications and measured composition (in wt.%).

Alloy	Spec.	C	Mo	Ni	P	Cr	Mn	Si	Fe
316L (UNS S31603)	Min		2.00	10.0		16.00			Balance
	Max	0.03	3.00	14.0	0.045	18.00	2.0	0.75	
316L (measured)		0.018	2.16	9.98	0.032	16.77	1.66	0.35	Balance
316H (UNS S31609)	Min	0.04	2.00	10.0		16.00			Balance
	Max	0.10	3.00	14.0	0.045	18.00	2.0	0.75	
316H (measured)		0.04	1.97	10	0.031	16.77	1.5	0.3	Balance

Table 2

Concentration of trace elements in FLiNaK salt used in this study as measured by ICP-MS before corrosion tests.

Element	Concentration (ppm)
Fe	78 ± 5
S	54 ± 3
P	10.3 ± 0.6
Ca	10 ± 3
Al	8.7 ± 0.5
Ni	4.0 ± 0.3
Cr	2.8 ± 0.1
Ti	0.8 ± 0.1
Mo	0.8 ± 0.1
Mn	0.70 ± 0.04

suspension of the specimens in the molten salt from a steel capsule lid using 316 stainless steel wire.

LiF-NaF-KF (46.5-11.5-42 mol %) salt was procured from Materion Corporation where it was mixed and melted in a graphite crucible in an argon environment. The initial LiF, NaF, and KF constituents each had a purity level of greater than 99.9 %. Differential scanning calorimetry (DSC) showed the salt's melting temperature to be 456 °C which is close to the theoretical eutectic temperature of the mixture of 454 °C [19]. Magnetic-sector inductively coupled plasma mass spectroscopy (ICP-MS) was used to measure the concentration of trace elements. The specific procedure for ICP-MS analysis was reported in our previous paper [17]. Table 2 shows the concentration of the trace impurities in the molten FLiNaK salt used in this study.

To investigate the influence of dissimilar materials on corrosion, each stainless steel was tested for corrosion in capsules of different materials. As shown in Fig. 1, several specimens of each stainless steel were exposed separately in capsules made of 316 stainless steel, nickel, pyrolytic boron nitride (PBN), or glassy carbon (GC). The 316 stainless steel and nickel (Ni-201 alloy) capsules were procured from Dynamic Temperature Supplies LLC. The metallic capsules had an inside diameter of 16 mm and a depth of 150 mm. A plug composed of the same material was welded on to the bottom of a tube using 316 stainless steel or nickel filler wire. The PBN capsules were procured from QS Advanced Materials Inc. These binder free PBN capsules were manufactured by CVD process and were of 99.99% purity. The PBN capsules had a lip diameter of 22 mm and depth of 141 mm. The 60 ml glassy (vitreous) carbon crucibles with a diameter of 37 mm and height of 80 mm were procured from SPI Supplies. All specimens were suspended from loosely fitting 316 stainless steel caps by 316 stainless steel wire.

2.2. Molten salt materials exposure tests

The samples were exposed to static molten FLiNaK salt for 500 h at 700 °C inside of an inert atmosphere glovebox where the moisture and oxygen concentrations were maintained below 2 ppm. Each capsule was loaded with 36 g of as-received FLiNaK salt. Using the density of pure FLiNaK reported by Williams [12] of

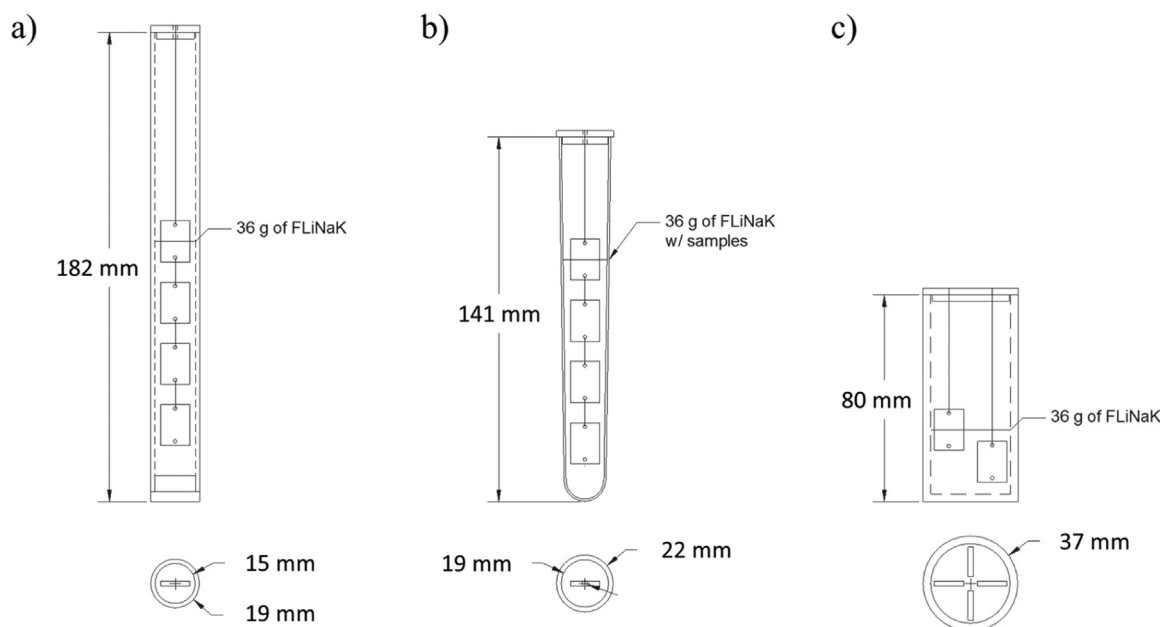


Fig. 1. Schematic diagram of (a) 316 stainless steel, (b) pyrolytic boron nitride (PBN), and (c) glassy carbon capsules showing test specimens suspended into the molten salt. Note that one sample was semi-submerged to allow for surface recession measurements using profilometry.

$2.530 - 0.00073 \cdot T[\text{°C}] \text{ g/cm}^3$, the calculated salt volume was approximately 17.8 mL at 700 °C. The salt was further dried inside the glovebox at 250 °C for 24 h to remove any potential residual moisture that may have been introduced into the salt during shipping. Specimens were introduced into the molten salt at the test temperature of 700 °C. Specimens were removed from the salt at temperature to eliminate any effects of re-plating of the corrosion products on the sample surface during cooling.

2.3. Materials characterization

Following exposure, the samples were ultrasonically cleaned in a 1M aluminum nitrate solution prior to characterization. The samples were vacuum dried at -25 inHg for 12 h. Then the masses of the specimens were measured using a Sartorius CPA26P high accuracy scale with a resolution of 2 µg. Sample dimensions were measured with a micrometer with a resolution of 0.01 mm. The weight change was calculated from the difference of the initial and final masses of the samples and normalized by the surface area of the sample. Weight change statistics were calculated from the average and standard deviation of three fully submerged coupons for each capsule.

Scanning electron microscopy (SEM) was performed using a Zeiss LEO 1530 in conjunction with compositional analysis conducted using a Thermo Scientific UltraDry energy dispersive spectroscopy (EDS) detector and Pathfinder software. The surface composition was evaluated using EDS area averages over areas of 0.25 mm² and EDS point scans with an diameter of 1 µm. The point scan data represents the average and standard deviation of three point-scans measured for both the matrix and precipitates.

Cross sections of the exposed samples were analyzed with EDS spectral maps and line scans. The spectral maps depict the distribution of the various alloying elements of interest and were used for evaluating grain boundary Cr dissolution, by measuring the maximum depth of selective Cr dissolution specifically along grain boundaries. The line scans were performed normal to the surface through the material bulk and analyzed to determine the bulk grain Cr dissolution as measured by the depth of selective Cr dissolution from within the grains. For all cross-sectional analyses, the samples were electroplated with copper before mounting in Bakelite

to promote edge retention during subsequent metallographic sample preparation.

Surface recession measurements were conducted on a fourth sample that was semi-submerged in the molten salt in each capsule by optical profilometry using a Zygo NewView 9000 scanning white light and optical phase-shifting interferometer. Line scans were performed vertically across the vapor-salt interface of the samples after the corrosion tests. The difference between the average heights of the surface exposed to the vapor phase and the surface exposed to the molten salt were used as a metric for surface recession.

X-ray Diffraction (XRD) was conducted with a Bruker D8 Discovery using CuKα radiation (1.542 Angstroms). In order to incorporate a statistically significant number of grains in each material, XRD was conducted over a broad 1 mm x 1mm area by oscillating the XRD stage at 0.2 mm sec⁻¹. The lattice parameter was measured using Bragg's law followed by Nelson-Riley extrapolation function ($\cos^2(\theta)/\sin(\theta) + \cos^2(\theta)/\theta$).

3. Results

3.1. Weight change after exposure to molten FLiNaK

In each capsule environment, 316L and 316H experienced varying amounts of weight loss when exposed to FLiNaK in different capsule materials. Fig. 2 summarizes the results of weight changes during these exposure tests. When exposed in 316L capsules, the weight changes of 316L and 316H were $-0.210 \pm 0.002 \text{ mg cm}^{-2}$ and $-0.119 \pm 0.001 \text{ mg cm}^{-2}$, respectively. In PBN capsules the two alloys had statistically the same weight change of $-1.5 \pm 0.1 \text{ mg cm}^{-2}$. Greater weight loss was observed for samples tested in glassy carbon capsules than in PBN capsules where the weight change of 316L and 316H were $-2.0 \pm 0.2 \text{ mg cm}^{-2}$ and $-1.7 \pm 0.1 \text{ mg cm}^{-2}$, respectively. The capsule material clearly had a significant effect on the weight loss due to corrosion.

3.2. Alloy surface morphology after molten salt exposure

The effect of molten salt exposure on the surface topography of the 316L and 316H exposed in various capsule materials was

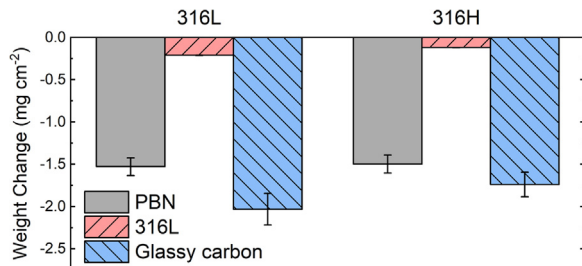


Fig. 2. Weight change for 316L and 316H stainless steels after exposure to FLiNaK for 500 h at 700 °C in pyrolytic boron nitride (PBN), 316 stainless steel (316L), and glassy carbon (GC) capsules.

examined with an SEM. The surface microstructure of the various samples is shown in Fig. 3. After exposure to FLiNaK in PBN and glassy carbon capsules, 316L and 316H showed clear evidence of grain boundary attack, indicative of preferential dissolution of alloying elements along grain boundaries. When exposed in 316L capsules, neither 316L nor 316H showed significant grain boundary attack, but instead, there was an emergence of facets on the surface. In addition to the facets, a uniform dispersion of second

phase particles emerged on the surface of the samples. It is speculated that the formation of these precipitate phases is promoted by depletion of elements, notably Cr, from the grains which alters the phase equilibria in the grains. Elemental analysis of the sample will be discussed in a later section. Comparison of the SEM images of the samples reveals significant differences between the mechanism of corrosion attack occurring in the different capsule environments. These modes of corrosion attack will be quantified in terms of uniform surface recession, preferential dissolution of elements from grain boundaries, and preferential dissolution of elements within the grains.

To investigate surface recession, profilometry was used to measure the surface topography and step-height of the vapor-salt interface for the semi-submerged samples. The results of 316L and 316H samples that were semi-submerged in PBN and glassy carbon capsules are shown in Fig. 4. The vapor-salt interface showed a sharp drop to a lower average surface height indicating uniform surface recession of the material due to corrosion. In the case of 316L and 316H exposed in PBN capsules and 316H exposed in glassy carbon, the interface was discrete and the step height could be readily measured. The surface recession measurement is the difference between the average surface heights of the area exposed to the

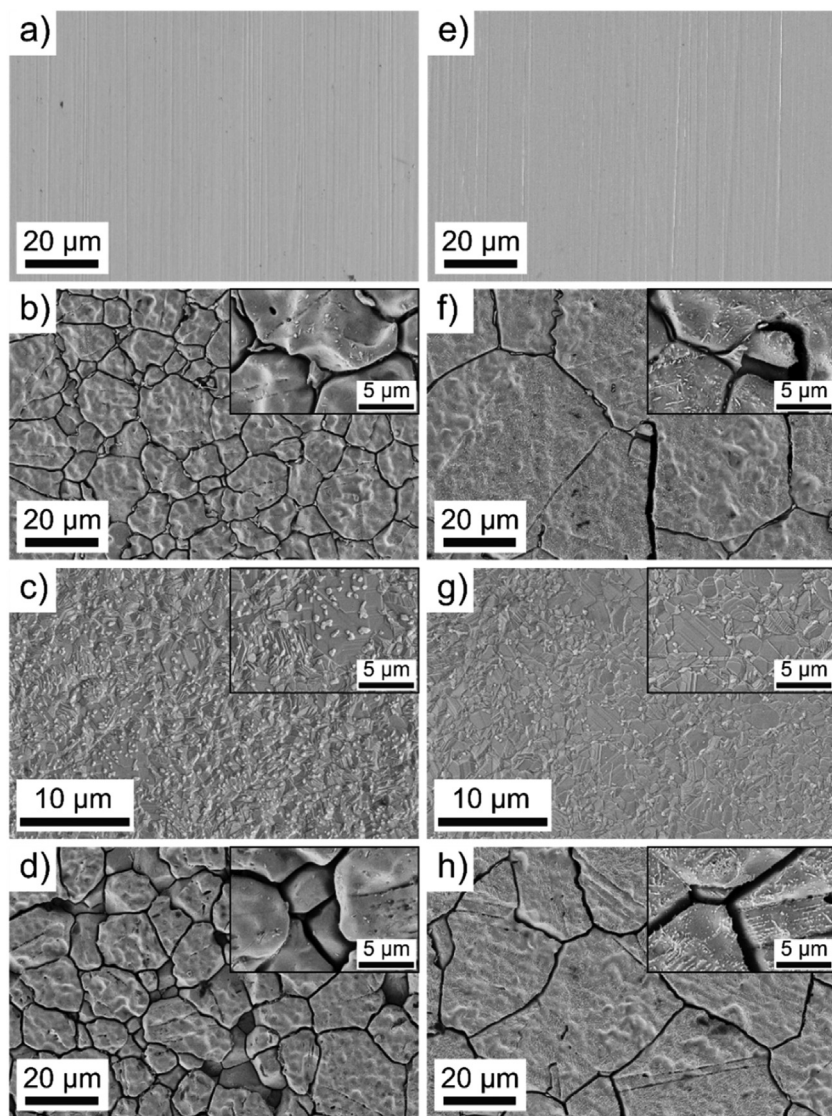


Fig. 3. SEM images of the surface of (a-d) 316L and (e-h) 316H (a),(e) before exposure, and after exposure to FLiNaK for 500 h at 700 °C in (b), (f) PBN capsules, (c), (g) 316L capsules, and (d), (h) in glassy carbon capsules.

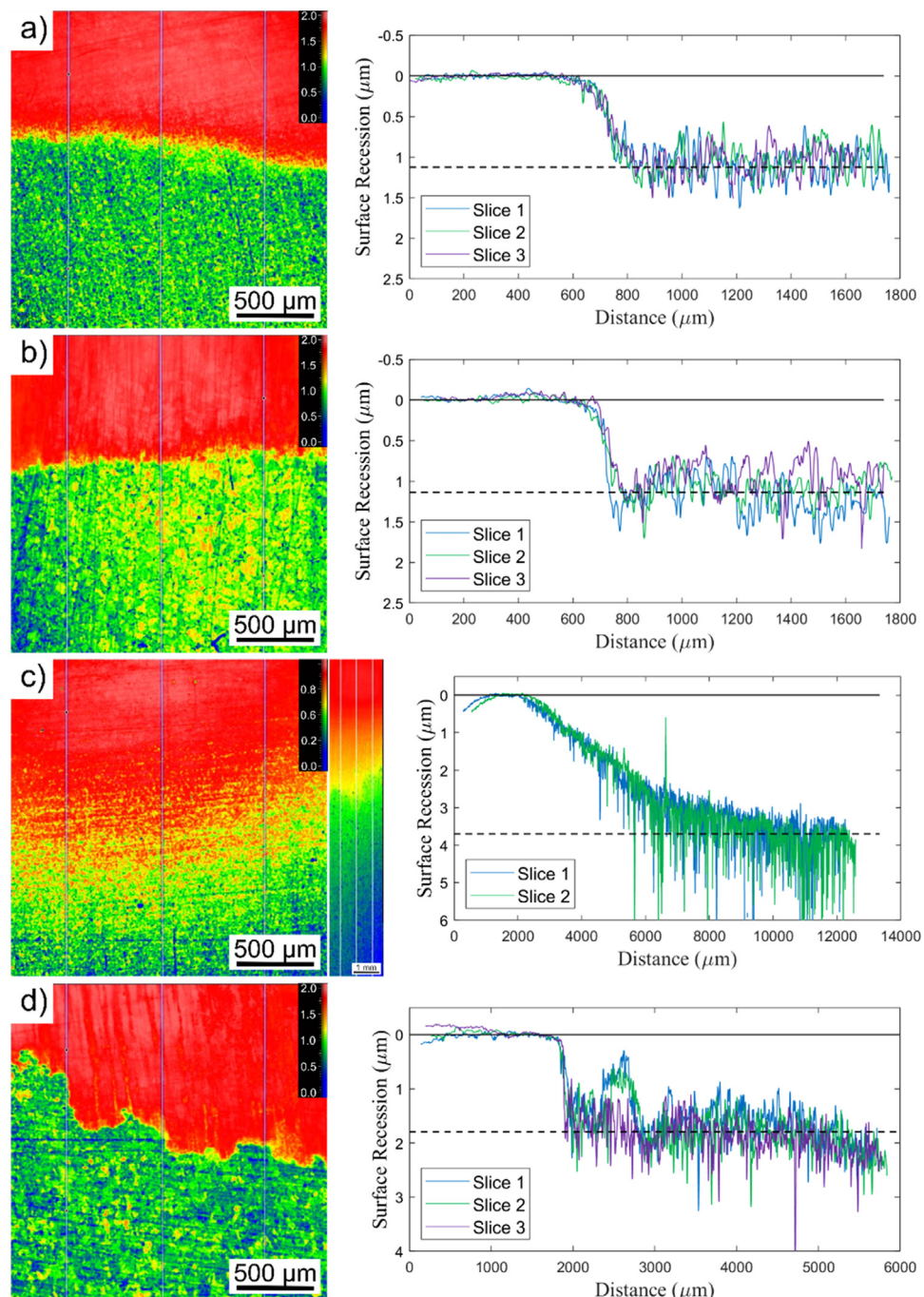


Fig. 4. Profilometry topographical maps and linear slice plots of the salt-vapor interface of (a) 316L in pyrolytic boron nitride (PBN), (b) 316H in pyrolytic boron nitride (PBN), (c) 316L in glassy carbon, and (d) 316H in glassy carbon. The bottom region (corresponding the right side of the profilometry scans) of the topographical map was submerged in molten salt and the top region was exposed to the vapor phase (units are in μm).

salt and the area exposed to the vapor phase where it is assumed that no removal of material due to corrosion has occurred. The surface recession of the 316L and 316H in PBN capsules were 1.13 μm and 1.14 μm , respectively. The surface recession of the 316L and 316H in glassy carbon capsules were 3.70 μm , 1.79 μm , respectively. For 316L samples in the glassy carbon capsule there was no sharp step at the interface, but rather the recession occurred gradually, as shown in Fig. 4(c). This required a broader scan comprised of several stitched profilometry measurements. It was not possible to quantify the surface recession of 316L or 316H exposed in 316 stainless steel capsules due to low corrosion rates which will be discussed later.

3.3. Elemental analysis of the corrosion surface

Compositional changes in the surface of the 316L and 316H samples were initially evaluated using EDS area average scans which yield the overall preferential dissolution of elements. Fig. 5 shows the composition of the surface of the as-received stainless steels and the net change in average composition of the surface after corrosion. In general, 316L showed a higher net decrease in Cr after exposure in all capsule environments, a result that is consistent with the relative higher weight loss measurements shown in Fig. 2. Relative enrichment of Ni and Mo was observed due to Cr dissolution. Both Ni and Mo have a low negative free energy of

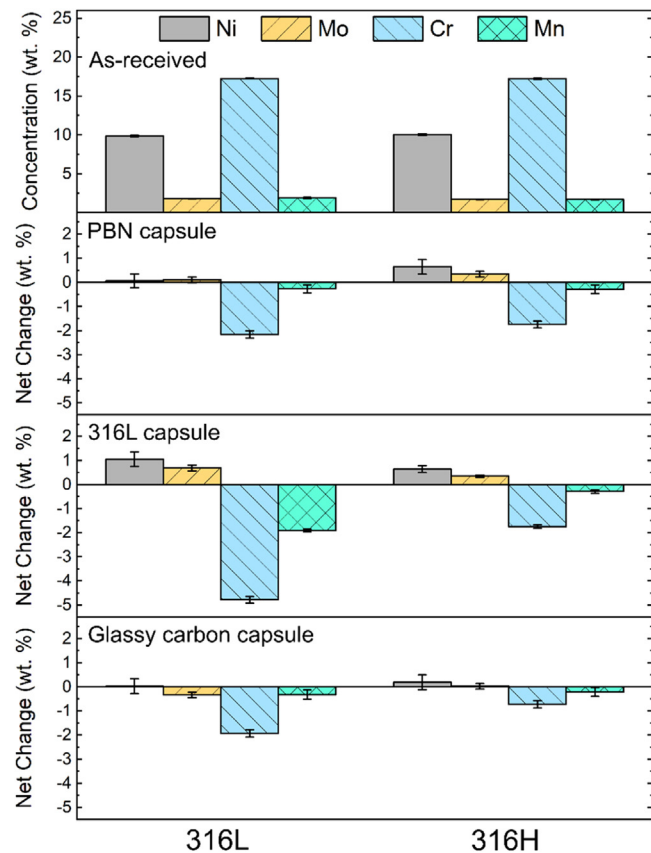


Fig. 5. EDS large area average compositional analysis of the as-received 316L and 316H specimens and the net change in composition after exposure to FLiNaK salt in different material capsules for 500 h at 700 °C. Fe makes up the balance of the composition.

fluoride formation. When exposed in 316 stainless steel capsules, the concentration of Mn decreased more in 316L specimens compared to the 316H specimens. Corrosion kinetics and transport of Mn in 316 stainless steel is lacking, but it has been shown that Mn is very susceptible to corrosion in fluoride salts [20].

The precipitate particles observed on the specimen surface after salt exposure in 316 stainless steel capsules were further investigated with SEM in Figs. 6. While accurate phase identification is challenging using XRD, point scans of the particles showed an enrichment of Mo up to 8 and 12 wt. %. Considering that the data from point scans incorporate the effects of the surrounding matrix, it was concluded that these particle phases are composed primarily of molybdenum. This result was consistent with the composition of the particles reported on the surface of 316L stainless steel after exposure to 2LiF-BeF₂ salt in 316 stainless steel capsules by Zheng et al. [8].

EDS cross-sectional analysis was performed on the samples to determine the most dominant modes of corrosion attack occurring in each capsule environment. Fig. 7 through Fig. 9 show the EDS spectral maps along with the distribution of Cr in the near surface region. It is noted here that the test temperature of 700 °C falls within the sensitization range of 316 stainless steel. Under these conditions, the chromium carbide phase forms at the grain boundaries [18]. The grain boundaries are highlighted in the Cr spectral maps indicating that sensitization had occurred. Consistent with this, the higher carbon 316H shows more continuous and thicker Cr-rich regions at the grain boundaries after corrosion testing. The depth of grain boundary Cr dissolution was measured by taking the maximum projected depth of the depleted grain boundary normal to the exposed surface. The yellow arrow in the SEM image indicates the path of the EDS line scan. The line scans are placed so that they extend from the Cu coating on the surface (deposited for edge retention) directly into the grains, avoiding the grain boundaries. The depth of bulk grain Cr dissolution is measured from the Cu coating interface (dotted line) to the approximate distance where the Cr approaches the bulk Cr concentration (dashed line).

When tested in PBN capsules, 316 stainless steels showed similar grain boundary Cr dissolution, but different bulk grain Cr dissolution. Fig. 7 shows grain boundary Cr dissolution for 316L and 316H to a depth of 5.8 μm and 6.3 μm, respectively. 316L did not show considerable Cr dissolution in the bulk grains. 316H, however, showed a depth of matrix Cr dissolution of 3 μm. The bulk grain Cr dissolution in 316H is consistent with the findings of EDS area averages which show relative enrichment in Mo and Ni due to the loss of Cr. In 316L, the majority of Cr is removed from the grain boundaries meaning that the composition of the surface grains remains relatively unaffected.

The cross sectional analysis of 316L and 316H exposed in 316L capsules did not show aggressive Cr dissolution. In Fig. 8, there was minimal grain boundary Cr dissolution in both materials. EDS line-scans, however, revealed dissolution of Cr in the bulk grains. The depths of bulk grain Cr dissolution in 316L and 316H were 6.0 μm and 3.0 μm, respectively. While the measured depth of bulk grain Cr dissolution is different, it should be noted that the apparent concentration of Cr at the surface of each alloy decreased to different levels. The total Cr dissolved, therefore, may be approximately the same in both alloys. It is speculated that since 316L may have more prevalent grain boundaries than 316H, the Cr in 316L may be transported from the bulk more rapidly via these kinetically favorable diffusion paths.

In contrast to experiments in 316L capsules, 316L and 316H specimens exposed in glassy carbon capsules experienced considerable dissolution of Cr along only the grain boundaries. In Fig. 9, the EDS line scans show that there is minimal depth of bulk grain Cr depletion. Instead, there is extensive dissolution of Cr from the grain boundaries that leaves considerable sized voids in the near-surface region. The depths of grain boundary Cr dissolution in 316L and 316H were 6.3 μm and 7.7 μm, respectively.

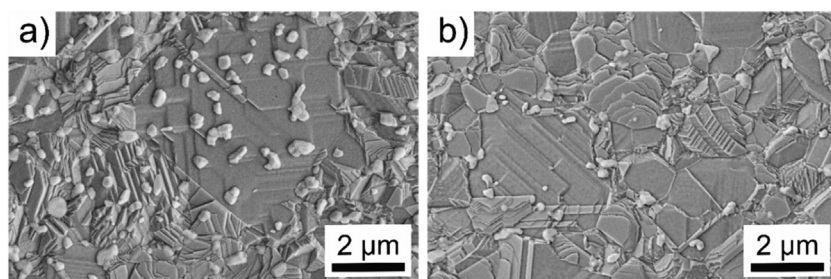


Fig. 6. High magnification SEM images of the surface of (a) 316L and (b) 316H exposed to FLiNaK in 316L capsules for 500 h at 700 °C.

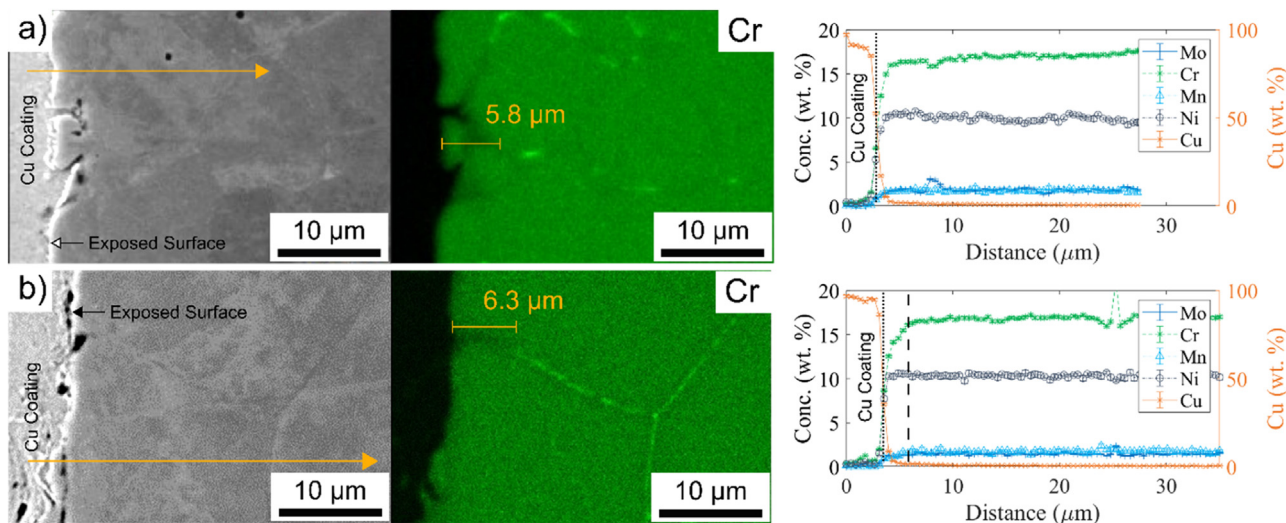


Fig. 7. Cross-sectional EDS compositional analysis of (a) 316L and (b) 316H surfaces exposed to FLiNaK in pyrolytic boron nitride (PBN) capsules for 500 h at 700 °C. A Cu coating was electroplated on the specimen surface for edge retention during subsequent metallographic preparation. Yellow arrow in the SEM image denotes the path of the EDS line scan.

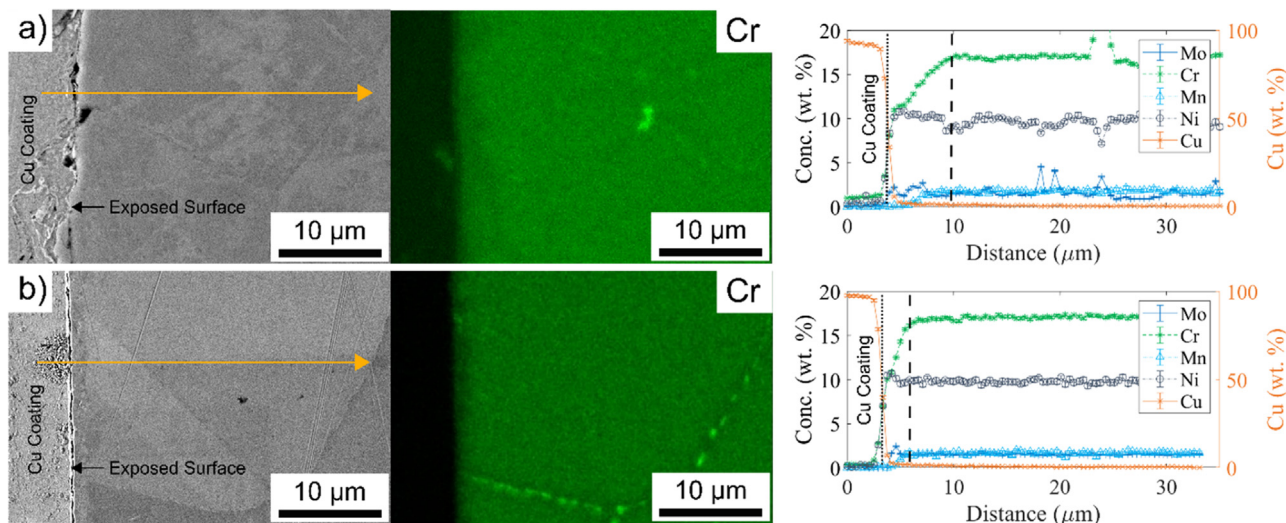


Fig. 8. Cross-sectional EDS compositional analysis of (a) 316L and (b) 316H surfaces exposed to FLiNaK in 316L capsules for 500 h at 700 °C. A Cu coating was electroplated on the specimen surface prior to mounting and polishing. Yellow arrow in the SEM image denotes the path of the EDS line scan.

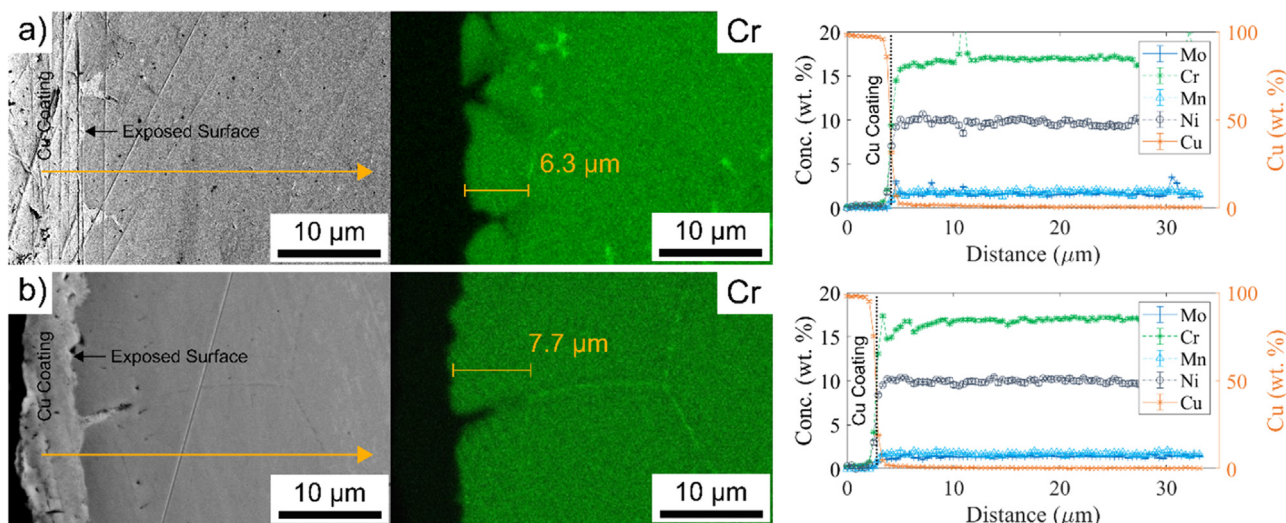


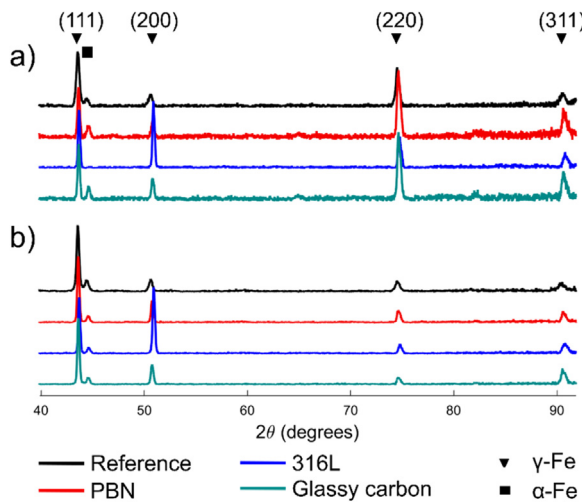
Fig. 9. Cross-sectional EDS compositional analysis of (a) 316L and (b) 316H surfaces exposed to FLiNaK in glassy carbon capsules for 500 h at 700 °C. A Cu coating was electroplated on the specimen surface prior to mounting and polishing. Yellow arrow in the SEM image denotes the path of the EDS line scan.

Table 3

Analysis of 316L and 316H corrosion after exposure to FLiNaK for 500 h at 700 °C in various capsule materials.

Specimen	Capsule	Weight Change (mg cm ⁻²)	RMS Surface Roughness (μm)	Surface Recession (μm)	Depth of Grain Boundary Cr Dissolution (μm)	Depth of Bulk Grain Cr Dissolution (μm)	Total Depth of Corrosion (μm)	Types of Corrosion
316L	PBN	-1.5 ± 0.1	0.496	1.13	5.8	0.0	6.9	Surface recession & grain boundary Cr dissolution
316H	PBN	-1.5 ± 0.1	0.392	1.14	6.3	3.0	7.5	Surface recession & grain boundary Cr dissolution
316L	316L	-0.210 ± 0.002	0.049	ND	0.0	6.0	6.0	Bulk grain Cr dissolution*
316H	316L	-0.119 ± 0.001	0.041	ND	0.0	3.0	3.0	Bulk grain Cr dissolution*
316L	Glassy carbon	-2.0 ± 0.2	0.925	3.70	5.8	0.0	9.5	Surface recession & grain boundary Cr dissolution
316H	Glassy carbon	-1.7 ± 0.1	0.497	1.79	7.7	0.0	9.5	Surface recession & grain boundary Cr dissolution

* It was not possible to quantify surface recession.

**Fig. 10.** XRD patterns for (a) 316L and (b) 316H reference samples and samples exposed to FLiNaK in pyrolytic boron nitride (PBN), 316L, and glassy carbon capsules for 500 h at 700 °C.

Three quantifiable metrics of corrosion attack were observed in 316 stainless steels in molten fluoride salt environments: surface recession (uniform corrosion), preferential elemental dissolution within the bulk grains, and preferential elemental dissolution along grain boundaries. **Table 3** summarizes the results obtained from this experiment. Total depth of corrosion attack is the cumulative effect of the measured surface recession and either the depth of grain boundary Cr dissolution or the depth of bulk grain Cr dissolution depending on which depth is greater.

3.4. XRD analysis of the corrosion surface

XRD was performed to identify the near-surface corrosion-induced changes in lattice parameter in the alloy microstructure due to exposure to molten salt. **Fig. 10** shows XRD patterns for 316L and 316H in both the as-received condition and after corrosion testing in PBN, 316L and glassy carbon capsules. Both 316L and 316H showed strong (111), (200), (220), and (311) γ -austenite peaks corresponding to the face-centered-cubic (FCC) bulk material. To precisely calculate the lattice parameter, Bragg's Law was first used to calculate the lattice parameter followed the use of the Nelson-Riley extrapolation function ($\cos^2(\theta)/\sin(\theta) + \cos^2(\theta)/\theta$) for the (200), (220), and (311) peaks of γ -austenite. In **Fig. 11**, the lattice parameter is obtained from the y-intercept of the linear fit to the data. The lattice parameters of as-received 316L and 316H were 360.13 pm and 360.05 pm, respectively. When Cr is depleted from

Table 4

Net change in lattice parameter of 316L and 316H specimens exposed in pyrolytic boron nitride (PBN), 316L, and glassy carbon capsules measured by Nelson-Riley function extrapolation. Units are in pm (picometers).

Sample	316L	316H
PBN	-0.49	-0.29
316L	-0.33	-0.11
Glassy Carbon	-0.12	-0.38

the austenite matrix, the alloy's lattice parameter is expected to shrink, due to the depletion of Cr from the γ -austenite solid solution and corresponding vacancy injection. The net change in lattice parameters of the exposed alloys were also calculated and are shown in **Table 4**. The lattice parameter of the γ -austenite phase decreases after exposure to molten salt which is consistent with the finding that the alloys experience some dissolution of Cr from the matrix.

Both materials in the as-received (reference) showed a faint peak around $2\theta = 45$ degrees corresponding to BCC ferritic phase. In most cases, this ferritic peak also exists in specimens after corrosion tests, despite the depletion of Cr which is a ferrite stabilizer. The presence of a ferrite peak after corrosion testing is an area of ongoing investigation, however a vacancy injection has been proposed to justify this observation [21]. It is not clear at this stage why the 316L specimens tested in 316L capsules shows no ferrite peaks.

3.5. Salt analysis

Salt compositional analysis using ICP-MS before and after exposure shows strong evidence of chromium dissolution. As shown in **Fig. 12**, the concentration of Cr increased in the salts exposed to the stainless steels. For both 316L and 316H, the salts recovered from the 316 stainless steel capsules showed the highest concentrations of Cr, a result of the lower salt volume to alloy surface area ratio. The concentration of Cr in the salts exposed in PBN capsules were comparable despite the difference in the modes of corrosion observed in 316L and 316H in these capsules.

As previously discussed, Mn is susceptible to corrosion in fluoride salts. In 316 stainless steel capsules containing 316L and 316H specimens, the concentration of Mn increased from less than 1 $\mu\text{g/g}$ to 61 $\mu\text{g/g}$ and 35 $\mu\text{g/g}$, respectively. In all other capsules, the concentration of Mn was consistently 13–15 $\mu\text{g/g}$. Even though Mn is a minor alloying element, it could show up in appreciable concentrations in fluoride salts contained in 316 stainless steel vessels.

Difficulty was encountered when quantifying other elements that might provide clues about the observed surface recession. The

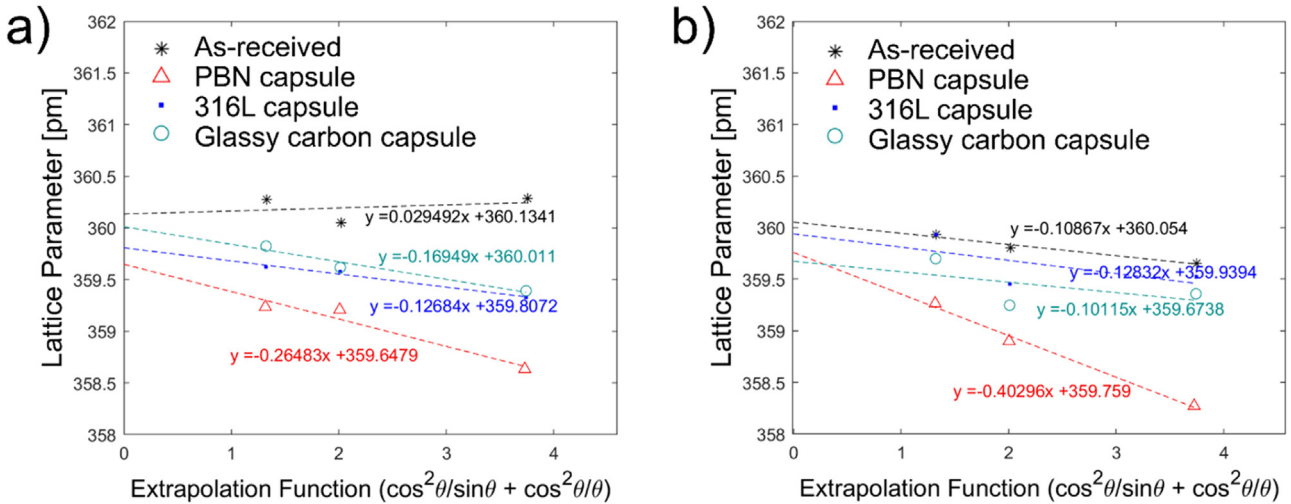


Fig. 11. Calculated lattice parameter as a function of the Nelson-Riley extrapolation function ($\cos^2(\theta)/\sin(\theta) + \cos^2(\theta)/\theta$) for (a) 316L and (b) 316H specimens exposed in different capsule materials.

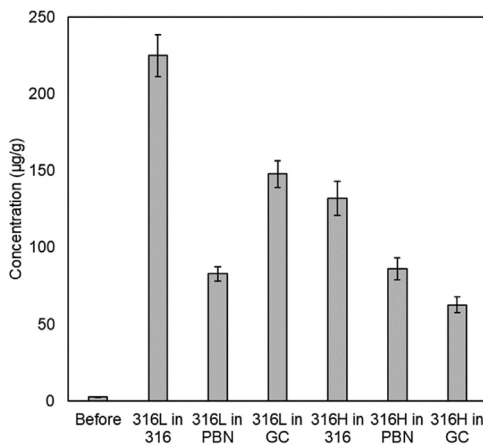


Fig. 12. The concentration of chromium in FLiNaK salt as determined by ICP-MS before and after exposure to 316L and 316H stainless steel in pyrolytic boron nitride (PBN), 316 stainless steel (316L), and glassy carbon (GC) capsules for 500 h at 700 °C.

concentrations of Ni and Mo remained lower than 1 $\mu\text{g/g}$ in all salts. The concentration of Fe in all the salts after exposure was approximately 4 $\mu\text{g/g}$. All ICP calibration standards were carefully validated for the elements reported. No undissolved compounds were observed in the digests. The measured plasma oxide formation was acceptably low. All matrix spikes, reference materials, and check standards were recovered for Fe ruling out matrix or isobaric interferences.

4. Discussion

An understanding of the modes of corrosion attack occurring in stainless steels in molten fluoride salts is essential for predicting their long-term corrosion performance. It also has implications for long-term mechanical performance due to wall thinning, and grain boundary attack (as observed in tests with glassy carbon capsules), and void formation (due to Kirkendall effect, as observed in tests with 316L capsules) in the near-surface regions of the material which could lead to stress-corrosion cracking and fatigue crack initiation. The competition between the observed modes of corrosion attack may present challenges for development of verifiable corrosion kinetic models. Through corrosion testing of alloys in dif-

ferent capsule environments it appears to be possible to isolate factors contributing to one mode of corrosion attack.

The stainless steels exposed in PBN capsules showed a combination of surface recession, preferential bulk grain Cr dissolution, and preferential grain boundary Cr dissolution. The non-conductive and inert nature of PBN is believed to mitigate the effects of galvanic and dissimilar materials corrosion, yet significant corrosion of 316 stainless steel occurred. There was no visible evidence of interaction between the PBN capsule and the salt or capsule and the specimen.

The specimens exposed in the 316 stainless steel capsules are important for establishing a corrosion behavior baseline for many contemporary flowing salt experiments. In these environments, the ratio of the salt volume to the surface area of the salt contacted vessel walls may be small. These specimens showed low weight loss and negligible surface recession. Instead, the main mode of corrosion attack was bulk grain Cr dissolution. This indicates that the corrosion process was mainly limited by diffusion of Cr from the bulk to the surface. Due to the specimen-capsule similarity, the inherent driving force for mass transport due to compositional differences is removed. These specimens showed significantly less weight loss than in other capsules despite the large increase in Cr concentration in the salt after exposure. Assuming a finite concentration of corrosive impurities in the salt, the attack is distributed over a larger surface area. This mitigated both surface recession and the weight loss in the test specimens. It is clear through comparison of the results from PBN and 316 stainless steel capsules that the volume of salt relative to the surface area of the corroding metal is an important factor in determining the rate and mode of corrosion attack.

An integral part of many reactor core designs, salt wetted graphite may have a unique influence on the corrosion resistance of the other salt contacting metal components. In glassy carbon capsules, 316 stainless steel showed relatively high surface recession and grain boundary Cr dissolution. Unlike in PBN capsules, no selective Cr dissolution in the bulk grains was observed. Graphite is cathodic with respect to stainless steel [22]. This may impose a sufficiently oxidizing redox condition to cause more rapid surface recession and possibly grain boundary Cr dissolution in the 316 stainless steels.

Environmental factors, such as dissimilar materials, and dynamic changes in salt/alloy chemistry are thought to have a significant influence on the observed modes of corrosion. In previous research by the authors [17], when the environment was made

more oxidizing by applying anodic potentials to metals and alloys with potentiodynamic polarization in FLiNaK, 316 stainless steel experienced more uniform surface recession than other alloys, such as the Ni-20wt.%Cr binary alloy. At sufficient oxidizing potentials, uniform surface recession became the dominant mode of corrosion attack for all alloys. It was observed that the anodic potential applied to the alloy relative to the inherent redox potential of the alloy's pure components was an important factor in determining whether the mode of corrosion attack was selective dealloying or uniform surface recession. Two environmental factors investigated in this work may explain the observed modes of corrosion attack. Dissimilar materials which form galvanic cells could impose a significant oxidizing redox condition on steel leading to more surface recession. Surface recession may also be common in high salt volume to metal surface area environments where the surface chemistry is rapidly changed by corrosion. Assuming the alloy's apparent redox potential is dominated by the redox reaction between the chromium metal and chromium fluoride, rapid depletion of Cr from surface may cause the apparent redox potential of the alloy to exceed the redox potential of iron leading to pronounced surface recession. In stainless steel capsules with low salt volume to surface area ratios, the net change of the more broadly distributed Cr depletion is smaller and consequently the alloys apparent redox potential may not rise as rapidly as in other environments. Thus, more of the original surface of the alloy is retained in the 316 stainless steel capsules.

In all capsules, 316L lost slightly more weight than 316H indicating that compositional or microstructural differences may be important factors in these environments. One possible explanation for the higher weight loss in 316L is its smaller grain size. 316L contained more salt facing grain boundaries than the 316H. If dissolution of Cr along grain boundaries dominates the mode of corrosion attack in the stainless steels, a greater prevalence of grain boundaries will provide more pathways for mass transport of Cr to the surface and therefore more weight loss. It is speculated that materials with smaller grain sizes may be prone to the formation of contiguous Cr depleted grain boundaries. Grains which are surrounded by grain boundary attack may become dislodged accelerating weight loss.

More corrosion of Cr was observed in 316L than in 316H when the specimens were exposed in 316L and glassy carbon capsules. The plan view EDS area averages and the salt analysis show a slightly higher net decrease in Cr concentration in 316L and corresponding increases in Cr concentration in the salt. This effect may be attributed to the higher degree of sensitization in 316H owing to its higher carbon concentration. This phenomenon is observed in the specimen cross section post exposure and denoted by the highlighted grain boundaries in the Cr EDS area maps. It is speculated that the effects of sensitization could be two-fold. First, the chromium carbide likely slows the diffusion of chromium along grain boundaries. Second, the chromium carbide may be more thermodynamically stable than elemental Cr at the grain boundaries. This contrasts with aqueous environments, where higher carbon contents in stainless steel results in a markedly lower corrosion resistance.

5. Conclusions

Corrosion testing of 316L and 316H stainless steels in molten FLiNaK salt at 700°C for 500 h was performed in 316L, pyrolytic boron nitride, and glassy carbon capsules. Comparison of the surface topography, composition, and near-surface microstructural changes in the two stainless steels revealed significant differences in corrosion mechanisms occurring in each capsule environment. The verification of surface recession of 316 stainless steel in fluoride salts may partially explain why much higher weight loss oc-

curs in iron-based alloys than in other alloys. A collective examination of the above results suggests that corrosion performance of 316H is slightly superior to 316L by some metrics and comparable by others. This is of considerable significance to the MSR application, given that, of the two materials, only 316H is ASME codified and can be utilized for the manufacture of structural components of MSRs. It was determined that PBN had the least influence on the inherent corrosion performance of the two stainless steels. In 316 stainless steel capsule environments with low salt volume to metal surface area ratios the corrosion attack by a finite number of corrosive impurities is distributed over a larger area leading to different modes of corrosion. Surface recession and grain boundary Cr dissolution were markedly suppressed, but more bulk grain Cr dissolution was observed. The glassy carbon capsules accelerated grain boundary attack. A closer examination of individual metrics for corrosion of the two materials revealed subtle microstructural differences. The difference in the average grain size of the two materials led to some stochastic uncertainties. The higher carbon content augmented the formation of chromium carbide phase at the grain boundaries as a result of sensitization that may contribute to the slightly improved corrosion resistance for 316H stainless steel.

Data availability

The raw/processed data required to reproduce these findings cannot be shared at this time as the data also forms part of an ongoing study.

William H. Doniger reports financial support was provided by US Department of Energy.

Declaration of Competing Interest

The authors declare that they have no known competing financial interests or personal relationships that could have appeared to influence the work reported in this paper.

CRediT authorship contribution statement

William Doniger: Conceptualization, Methodology, Investigation, Formal analysis, Writing – review & editing. **Cody Falconer:** Conceptualization, Writing – review & editing. **Adrien Couet:** Conceptualization, Writing – review & editing. **Kumar Sridharan:** Conceptualization, Writing – review & editing, Supervision.

Acknowledgements

This work was supported by the U.S. Department of Energy Nuclear Energy University Program under contract No. DE-NE0008803. The authors gratefully acknowledge the use of facilities and instrumentation at the UW-Madison Wisconsin Centers for Nanoscale Technology (wcnt.wisc.edu) partially supported by the NSF through the University of Wisconsin Materials Research Science and Engineering Center (DMR-1720415).

References

- [1] Generation IV nuclear reactors, World Nucl. Assoc. (2017) Dec.[Online]. Available <http://www.world-nuclear.org/information-library/nuclear-fuel-cycle/nuclear-power-reactors/generation-iv-nuclear-reactors.aspx>.
- [2] "BPVC Section III-Div 5 - high temperature reactors - ASME." <https://www.asme.org/codes-standards/find-codes-standards/bpvc-iii-5-bpvc-section-iii-rules-construction-nuclear-facility-components-division-5-high-temperature-reactors> (accessed Feb. 13, 2022).
- [3] J. Koger, "Chromium depletion and void formation in Fe-Ni-Cr alloys during molten salt corrosion and related processes," *Chromium Deplet. Void Form. Fe-Ni-Cr Alloys Molten Salt Corros. Relat. Process.*, 1974.
- [4] J. Zhang, C. Forsberg, M. Simpson, S. Guo, S. Lam, R. Scarlat, F. Carotti, K. Chan, P. Singh, W. Doniger, K. Sridharan, J. Keiser, Redox potential control in molten salt systems for corrosion mitigation, *Corros. Sci.* 144 (2018) 44–53 Nov., doi:[10.1016/j.corsci.2018.08.035](https://doi.org/10.1016/j.corsci.2018.08.035).

- [5] W.R. Grimes, Molten-salt reactor chemistry, *Nucl. Appl. Technol.* 8 (1970) 137–155 Feb..
- [6] S.S. Raiman, S. Lee, Aggregation and data analysis of corrosion studies in molten chloride and fluoride salts, *J. Nucl. Mater.* 511 (2018) 523–535 Dec., doi:[10.1016/j.jnucmat.2018.07.036](https://doi.org/10.1016/j.jnucmat.2018.07.036).
- [7] J. Keiser, J. Devan, Corrosion resistance of type 316 stainless steel to Li_2BeF_4 , *Am. Nucl. Soc. Trans.* 22 (1975) 160 1975.
- [8] G. Zheng, L. He, D. Carpenter, K. Sridharan, Corrosion-induced microstructural developments in 316 stainless steel during exposure to molten Li_2BeF_4 (FLiBe) salt, *J. Nucl. Mater.* 482 (2016) 147–155 Dec., doi:[10.1016/j.jnucmat.2016.10.023](https://doi.org/10.1016/j.jnucmat.2016.10.023).
- [9] J. Qiu, B. Leng, H. Liu, D. Macdonald, A. Wu, Y. Jia, W. Xue, G. Yu, X. Zhou, Effect of SO_4^{2-} on the corrosion of 316L stainless steel in molten FLiNaK salt, *Corros. Sci.* 144 (2018) 224–229 Nov., doi:[10.1016/j.corsci.2018.08.057](https://doi.org/10.1016/j.corsci.2018.08.057).
- [10] S.W. McAlpine, N.C. Skowronski, W. Zhou, G. (Tony) Zheng, M.P. Short, Corrosion of commercial alloys in FLiNaK molten salt containing EuF₃ and simulants fission product additives, *J. Nucl. Mater.* 532 (2020) 151994 Apr., doi:[10.1016/j.jnucmat.2020.151994](https://doi.org/10.1016/j.jnucmat.2020.151994).
- [11] C. Sona, B. Gajbhiye, P. Hule, A. Patwardhan, C. Mathpati, A. Borgohain, N. Makhshwari, High temperature corrosion studies in molten salt-FLiNaK, *Corros. Eng. Sci. Technol.* 49 (4) (2014) 287–295 Jun., doi:[10.1179/1743278213Y.0000000135](https://doi.org/10.1179/1743278213Y.0000000135).
- [12] M. Kondo, T. Nagasaka, Q. Xu, T. Muroga, A. Sagara, N. Noda, D. Ninomiya, M. Nagura, A. Suzuki, T. Terai, N Fujii, Corrosion characteristics of reduced activation ferritic steel, JLF-1 (8.92Cr–2W) in molten salts Flibe and Flinak, *Fusion Eng. Des.* 84 (7–11) (2009) 1081–1085 Jun., doi:[10.1016/j.fusengdes.2009.02.046](https://doi.org/10.1016/j.fusengdes.2009.02.046).
- [13] L.C. Olson, R. Fuentes, M. Martinez-Rodriguez, J. Ambrosek, K. Sridharan, M. Anderson, B. Garcia-Diaz, J. Gray, T. Allen, Impact of corrosion test container material in molten fluorides, *J. Sol. Energy Eng.* 137 (6) (2015) 061007 Dec., doi:[10.1115/1.4031682](https://doi.org/10.1115/1.4031682).
- [14] H. Sun, X. Ding, H. Ai, G. Lei, X. Yang, J.Q. Wang, Interaction mechanisms of a Hastelloy N-316L stainless steel couple in molten LiF-NaF-KF salt, *Corros. Sci.* 164 (2020) 108317 Mar., doi:[10.1016/j.corsci.2019.108317](https://doi.org/10.1016/j.corsci.2019.108317).
- [15] C. Falconer, W. Doniger, L. Bailly-Salins, E. Buxton, M. Elbakshwan, K. Sridharan, A. Couet, Non-galvanic mass transport in molten fluoride salt isothermal corrosion cells, *Corros. Sci.* 177 (2020) 108955 Dec., doi:[10.1016/j.corsci.2020.108955](https://doi.org/10.1016/j.corsci.2020.108955).
- [16] S.S. Raiman, J.M. Kurley, D. Sulejmanovic, A. Willoughby, S. Nelson, K. Mao, C. Parish, M.S. Greenwood, B. Pint, Corrosion of 316H stainless steel in flowing FLiNaK salt, *J. Nucl. Mater.* 561 (2022) 153551 Apr., doi:[10.1016/j.jnucmat.2022.153551](https://doi.org/10.1016/j.jnucmat.2022.153551).
- [17] W.H. Doniger, A. Couet, K. Sridharan, Potentiodynamic polarization of pure metals and alloys in molten LiF-NaF-KF (FLiNaK) using the K/K⁺ dynamic reference electrode, *J. Electrochem. Soc.* 169 (7) (2022) 071502 Jul., doi:[10.1149/1945-7111/ac7a66](https://doi.org/10.1149/1945-7111/ac7a66).
- [18] H. F. Ebliing and M. A. Scheil, "Time-Temperature-Sensitization (TTS) diagrams for types 347, 304L, and 316L stainless steels," in *Advances in the Technology of Stainless Steels and Related Alloys*, Committee A-10, Ed. 100 Barr Harbor Drive, PO Box C700, West Conshohocken, PA 19428-2959: ASTM International, 1965, pp. 275–275–10, doi:[10.1520/STP43752S](https://doi.org/10.1520/STP43752S).
- [19] D. F. Williams, "Assessment of Candidate Molten Salt Coolants for the Advanced High-Temperature Reactor (AHTR)," Oak Ridge National Laboratory, ORNL/TM-2006/12, 2006. [Online]. Available: <https://info.ornl.gov/sites/publications/Files/Pub57476.pdf>
- [20] M. Elbakshwan, W. Doniger, C. Falconer, M. Moorehead, C. Parkin, C. Zhang, K. Sridharan, A. Couet, Corrosion and thermal stability of CrMnFeNi high entropy alloy in molten FLiBe salt, *Sci. Rep.* 9 (1) (2019) Dec., doi:[10.1038/s41598-019-55653-2](https://doi.org/10.1038/s41598-019-55653-2).
- [21] Y. Wang, B. Goh, P. Nelaturu, T. Duong, N. Hassan, R. David, M. Moorehead, S. Chaudhuri, A. Creuziger, J. Hattrick-Simpers, D. Thoma, K. Sridharan, A. Couet, "Accelerated discovery of molten salt corrosion-resistant alloy by high-throughput experimental and modeling methods coupled to data analytics," *arXiv:2104.10235 [cond-mat, physics:physics]*, Apr. 2021, Accessed: Feb. 02, 2022. [Online]. Available: <http://arxiv.org/abs/2104.10235>
- [22] J. Qiu, A. Wu, Y. Li, Y. Xu, R. Scarlat, D.D. Macdonald, Galvanic corrosion of Type 316L stainless steel and graphite in molten fluoride salt, *Corros. Sci.* (2020) 108677 Apr., doi:[10.1016/j.corsci.2020.108677](https://doi.org/10.1016/j.corsci.2020.108677).